

Atomic displacements in the “charge-ice” pyrochlore $\text{Bi}_2\text{Ti}_2\text{O}_6\text{O}'$ studied by neutron total scattering

Daniel P. Shoemaker* and Ram Seshadri
*Materials Department and Materials Research Laboratory,
 University of California, Santa Barbara, CA, 93106, USA*

Andrew L. Hector
School of Chemistry, University of Southampton, Highfield, Southampton SO17 1BJ, UK

Anna Llobet and Thomas Proffen
*Los Alamos National Laboratory, Lujan Neutron Scattering Center,
 MS H805, Los Alamos, New Mexico 87545, USA*

Craig J. Fennie
School of Applied and Engineering Physics, Cornell University, Ithaca, New York 14853, USA
 (Dated: October 31, 2018)

The oxide pyrochlore $\text{Bi}_2\text{Ti}_2\text{O}_6\text{O}'$ is known to be associated with large displacements of Bi and O' atoms from their ideal crystallographic positions. Neutron total scattering, analyzed in both reciprocal and real space, is employed here to understand the nature of these displacements. Rietveld analysis and maximum entropy methods are used to produce an average picture of the structural non-ideality. Local structure is modeled *via* large-box reverse Monte Carlo simulations constrained simultaneously by the Bragg profile and real-space pair distribution function. Direct visualization and statistical analyses of these models show the precise nature of the static Bi and O' displacements. Correlations between neighboring Bi displacements are analyzed using coordinates from the large-box simulations. The framework of continuous symmetry measures has been applied to distributions of $\text{O}'\text{Bi}_4$ tetrahedra to examine deviations from ideality. Bi displacements from ideal positions appear correlated over local length scales. The results are consistent with the idea that these nonmagnetic lone-pair containing pyrochlore compounds can be regarded as highly *structurally* frustrated systems.

PACS numbers: 61.05.fm, 61.43.Bn, 75.10.Jm

I. INTRODUCTION

Magnetic oxides with the $A_2B_2O_7$ pyrochlore structure have been the subject of intense study. The lattice of corner-connected tetrahedra of A atoms hinders cooperative magnetic ordering, and when the A atom spins are Ising, an ice-like ground state is produced, for example in $\text{Dy}_2\text{Ti}_2\text{O}_7$ and $\text{Ho}_2\text{Ti}_2\text{O}_7$.¹⁻⁴ Other recent developments in oxide pyrochlores include superconductivity in osmium compounds,⁵ the formation of polar metallic states with unusual phonon modes,⁶ and the suggestion of chiral magnetic ground states.⁷ The analogy between Ising spins and vector displacements of cations within their coordination polyhedra has led to the suggestion that polar ordering may be similarly frustrated on the pyrochlore lattice.⁸ Thus in pyrochlore $\text{Bi}_2\text{Ti}_2\text{O}_6\text{O}'$, it is known that the Bi^{3+} atoms, usually predisposed to off-centering within their coordination polyhedra, display incoherent displacements permitting the average structure to remain cubic.⁹ This is in sharp contrast to the Bi^{3+} -containing perovskites BiMnO_3 and BiFeO_3 where the lone-pair active A-site produces polar, non-cubic ground states.¹⁰ Some signatures of these incoherent displacements are seen in measurements of heat capacity of $\text{Bi}_2\text{Ti}_2\text{O}_6\text{O}'$ and related compounds at low

temperatures.¹¹

Significant advances in describing frustrated, ice-like behavior in magnetic pyrochlores have been made when atomistic models are utilized to describe the interactions between individual A sites. For example, atomistic simulation of magnetic spin ordering in $\text{Dy}_2\text{Ti}_2\text{O}_7$ leads to a picture of localized, uncompensated spins connected by strings of ordered spins.^{3,4} This picture is local: spin behavior is driven by connectivity, geometry, and pairwise exchange interactions. However, it also agrees with bulk thermodynamic measurements: the heat capacity of the ensemble average agrees with experimental observations. We show here that experimental modeling over multiple length scales, both atomistic and averaged, affords a view of the pyrochlore $\text{Bi}_2\text{Ti}_2\text{O}_6\text{O}'$ where Bi *displacements*, rather than spins, form a frustrated network on the A sublattice.

$\text{Bi}_2\text{Ti}_2\text{O}_6\text{O}'$ [structure in Fig. 1(a)] is written thus to emphasize the two sublattices: one of corner-sharing TiO_6 octahedra, and the other of corner-sharing $\text{O}'\text{Bi}_4$ tetrahedra. While the TiO_6 sublattice is rigid in models of the average structure, Bi atoms are suggested to displace 0.4 \AA normal to the linear $\text{O}'\text{-Bi-O}'$ bond in an uncorrelated manner.^{8,9} First-principles calculations on $\text{Bi}_2\text{Ti}_2\text{O}_6\text{O}'$ predict Bi displacements but these

are perforce associated with non-cubic symmetries.¹² Diffuse intensity in electron diffraction patterns of related compounds including $\text{Bi}_2\text{Ru}_2\text{O}_7$, $\text{Bi}_2\text{InNbO}_7$, and $\text{Bi}_2\text{ScNbO}_7$ may indicate short-range correlations in the Bi displacements.^{13–15} If Bi displacements cooperatively order with each other, they must do so only over short ranges. Crystallographic analysis based on Bragg scattering leaves a void in the ability to probe such short-range order, as analyses are predicated on the existence of long-range order. Consequently, studies of displacive disorder on the *A* site *via* Rietveld refinement or Fourier maps can produce a model of the *average* electron or nuclear distributions, but each *A* site has an identical cloud of intensity.¹⁶

We investigate models where the correlated motion of atoms on the *A* sites reproduces the atomistic, pairwise distances between individual atoms. This description is provided by an appropriate Fourier transform of the total scattering function $S(Q)$ to provide a normalized pair distribution function (PDF).^{17,18} In this study, the PDF and the Bragg profile are used as experimental constraints in a large-box (11,000 atom) model of $\text{Bi}_2\text{Ti}_2\text{O}_6\text{O}'$ to obtain, using reverse Monte-Carlo (RMC) analysis, a consistent picture of the the coordination tendencies of all atoms. Many of these models are combined and used as a set of atomic positions for further analysis. RMC compares the experimental and computed (based on atom positions in the simulation box) $D(r)$ and $S(Q)$ while randomly relaxing atomic positions. The method is similar to Metropolis Monte Carlo, except that the fit to data χ^2 , instead of a potential energy function, is minimized.^{19–21}

There are many approaches to describing the behavior and correlations of atomic positions as obtained from large-box models of structure. Some examples include the use of quadrupolar moments of octahedra to describe LaMnO_3 ,²² of contour plots of bond angles in cristobalite,²³ and the use of bond valence analysis to obtain valence states from a statistical analysis of metal-oxygen positions.^{24,25} Here we analyze the local geometry using simple metrics, then present the continuous symmetry measures (CSM)^{26–28} of polyhedra from RMC simulations. The CSM model provides a quantitative measure of a polyhedron’s distortion, in the form of a “distance” from ideality. A key advantage of CSM is its ability to compare shapes in different compounds.²⁸ The CSM has been used to correlate deviations from ideal tetrahedra in silicates as a function of applied pressure,²⁹ and to analyze second-order Jahn-Teller systems across a variety of crystal structures.³⁰ In these cases, the CSM was considered for the average crystallographic structure, *e.g.* one where polyhedra possess a single CSM value. Here, we extend CSM to large-box modeling by calculating it for every $\text{O}'\text{Bi}_4$ tetrahedron in the RMC supercell, obtaining distributions, rather than single values.

The key finding to emerge from this study is that displacements from ideal atomic positions in $\text{Bi}_2\text{Ti}_2\text{O}_6\text{O}'$ and in particular, the nature of the $\text{O}'\text{Bi}_4$ tetrahedra indicate a tendency for Bi to lie in a disordered ring around

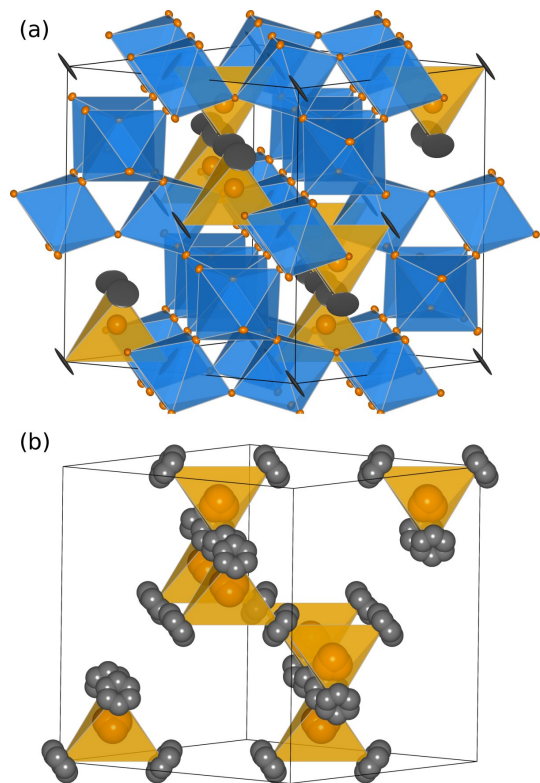


FIG. 1: (Color online) The $\text{Bi}_2\text{Ti}_2\text{O}_6\text{O}'$ crystal structure is shown in (a), with 50% thermal ellipsoids representing the atomic displacement parameters from Rietveld refinement at 14 K. The two sublattices are corner-sharing TiO_6 octahedra (blue) and corner-sharing $\text{O}'\text{Bi}_4$ tetrahedra (orange). Bi and O' are on ideal positions. Bi cations (black) appear as discs due to their displacement normal to the $\text{O}'\text{-Bi-O}'$ bond. This disorder can be modeled using six-fold-split Bi and four-fold-split O' as shown in (b) (only the $\text{O}'\text{Bi}_4$ is sublattice shown).

the ideal position, with some preference for near-neighbor Bi-Bi ordering. This reaffirms the case that, even when probed microscopically, $\text{Bi}_2\text{Ti}_2\text{O}_6\text{O}'$ is ice-like in its disorder. We emphasize that in drawing the analogy with ice, we do not suggest the existence of ice-rules of the Bernal-Fowler³¹ type in these systems.

II. METHODS

Synthesis and a detailed average structural analysis of the sample used in this study (including verification of purity) has been reported by Hector and Wiggin.⁹ Briefly, a basic solution of titanium metal with hydrogen peroxide and ammonia was added to an acidic solution of bismuth nitrate pentahydrate and nitric acid. The resulting precipitate was filtered, washed with a dilute ammonia solution, dried at 50°C , and calcined in air for 16 h at 470°C . Time-of-flight (TOF) neutron powder diffraction on samples held in vanadium cans was collected at the NPDF instrument at Los Alamos National Laboratory at 298 K

and 14 K. NPDF is designed to collect high-resolution, high-momentum-transfer data suitable for production of the PDF, as well as traditional Rietveld refinement. We performed Rietveld refinement using GSAS.³² Extraction of the PDF with PDFGetN³³ used $Q_{max} = 35 \text{ \AA}^{-1}$, and least-squares refinements of the PDF were performed with PDFgui.³⁴

First-principles density functional methods were used to identify a possible ordered ground state. The local stability of $Fd\bar{3}m$ $\text{Bi}_2\text{Ti}_2\text{O}_7$ was investigated using projector augmented wave potentials within the local density approximation as implemented in the VASP program^{35–38} and described previously.¹² We found three zone-center lattice instabilities—one ferroelectric and two antiferroelectric-like modes—which were used to guide a systematic search for low-symmetry phases. We performed a series of structural relaxations within each of the highest-symmetry isotropy subgroups^{39,40} consistent with the freezing-in of one or more of these lattice instabilities. We found that the lowest energy structure is ferroelectric (with a substantial polarization of $\mathbf{P} \approx 20 \mu\text{C cm}^{-2}$), in the polar monoclinic space group Cm , consistent with the freezing-in of all three modes.

Maximum entropy method (MEM) calculations of the nuclear scattering density were performed using PRIMA.⁴¹ RMC simulations were performed using RMCProfile⁴² version 6 on a $5 \times 5 \times 5$ supercell (cubic, $\approx 52 \text{ \AA}$ per side) with 11000 atoms. These simulations were constrained by the PDF (in the form of $D(r)$)⁴³ up to $r = 12 \text{ \AA}$ and by the Bragg profile of NPDF bank 1, which contains the lowest- Q Bragg reflections. Crystal structures are visualized using VESTA⁴⁴ and AtomEye.⁴⁵ Quantitative analyses shown in this work are taken from averaging many simulations in order to obtain an unbiased interpretation of the fit to data. Hard-sphere cutoffs were employed in RMC simulations to ensure that atoms did not approach closer than the specified nearest-neighbor distances, but no bunching was observed at these cutoffs. CSM for $\text{O}'\text{Bi}_4$ tetrahedra were calculated using a distance measure program provided by M. Pinsky and D. Avnir.

III. RESULTS AND DISCUSSION

A. Average structure from Rietveld refinement

The profile resulting from TOF neutron Rietveld refinement is displayed (for a single bank of data) in Fig. 2. The goodness of fit parameter $R_{wp} = 2.9\%$. The sample is the same as used in the Rietveld study of Hector and Wiggin,⁹ and the fit converges to similar structural parameters (within error), so these will not be reproduced here.

In $\text{Bi}_2\text{Ti}_2\text{O}_6\text{O}'$, preliminary Rietveld refinement using an ideal pyrochlore model can obtain a good fit to data, but large atomic displacement parameters (ADPs) indicate that significant atomic disorder is present, character-

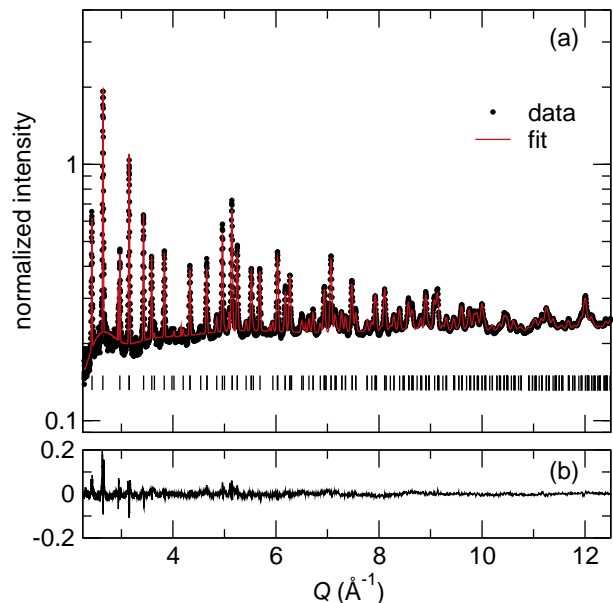


FIG. 2: (Color online) Neutron TOF Rietveld refinement of $\text{Bi}_2\text{Ti}_2\text{O}_6\text{O}'$ at 14 K (a) using the model of Hector and Wiggin⁹ gives a fit with $R_{wp} = 2.9\%$. Small features in the difference curve (b) at low Q are caused by shoulders of diffuse intensity around Bragg peaks. This component of the data can be interpreted using total scattering analysis.

ized by an elliptical spread around the ideal atomic positions. The ideal Bi position on the $16c$ (0,0,0) site can be fit using a large U_{23} component. These appear as large, flat discs in Fig. 1(a) with a radius of about 0.4 \AA . The discs envelop the Bi displacive disorder which we seek to accurately describe. The O' atoms at the $8a$ ($\frac{1}{8}, \frac{1}{8}, \frac{1}{8}$) position have large, isotropic displacements as well, corresponding to $U_{iso} \approx 0.4 \text{ \AA}^2$. The TiO_6 sublattice, on the other hand, is described by small U_{iso} values and does not display any signs of displacive disorder. Here we investigate the precise nature of atomic displacements in the $\text{O}'\text{Bi}_4$ sublattice.

Improved refinement of the average pyrochlore structure has been achieved by using a split-atom model for the A sites, such as in studies of $\text{Bi}_2\text{Ti}_2\text{O}_6\text{O}'$,^{9,46} $\text{Bi}_2\text{Sn}_2\text{O}_7$,⁴⁷ or $\text{La}_2\text{Zr}_2\text{O}_7$.¹⁶ Hector and Wiggin modeled Bi using a six-fold ring in the $96g$ position,⁹ but acknowledged that their refinement does not clearly show a preference for $96g$ versus $96h$ (rotated 30° to each other). The $96g$ split-atom configuration is shown in Fig. 1(b). Comparison to an ideal-position model in Fig. 1(a) shows that the Bi split-atom sites lie inside the anisotropic discs. Most O' intensity is still centered on the $8a$ site, but some occupancy is shifted away in 4 directions to form a tetrapod, modeled by partial occupancy of the $32e$ sites. From Rietveld refinement, we find that the Bi displacement parameters at 14 K and 300 K are similar in orientation and magnitude. This suggests that Bi displacements are frozen at room (and higher) temperatures, and what is being monitored in the scattering is not a

snapshot of dynamic motion, but rather a description of static positions. The suggestion of frozen displacements at room temperature is consistent with measurements of the temperature- and field-dependence of the dielectric constant in $\text{Bi}_2\text{Ti}_2\text{O}_6\text{O}'$ thin films.⁴⁸

Kinks in the difference profiles of the Rietveld refinement in Fig. 2(b) can be attributed to shoulders of diffuse intensity around low- Q peaks. The diffuse scattering cannot be interpreted here because the Rietveld technique only models Bragg intensity. Crucial approximations are made to model a structure using only Bragg peaks: we must average any atomic correlations or distortions that do not possess long-range ordering. The Bi distortions are incoherent, and their description will require an examination of diffuse scattering. Total scattering analysis of the real-space PDF, discussed here subsequently, provides a real-space tool to model both Bragg and diffuse scattering simultaneously.

B. Maximum entropy method

The maximum entropy method (MEM) is used here to produce a map of neutron scattering density in the unit cell. The method, proposed originally by Jaynes,^{49,50} uses some testable information (in this case, observed Bragg peak intensities in TOF neutron diffraction), and is based on the most probable distribution (nuclear scattering density) being the one with the largest information entropy. This method is described by Sakata^{51,52} and in the context of the MEM software program MEED,⁵³ a precursor to the software code PRIMA used here. The MEM input consists of the observed Bragg structure factor F_{obs} (from a Le Bail fit, with phase information from the ideal structure) for a list of hkl reflections, the unit cell dimensions, space group, and the sum of all scattering lengths in the cell. The MEM as employed here is largely model-free in the sense that atomic positions are not specified during the calculation, but phase information for F_{obs} is biased by the ideal structure. The final result is required to obey the symmetry of the space group. This is also an average structure probe—diffuse scattering intensity is ignored. Thus all Bi atomic positions in $\text{Bi}_2\text{Ti}_2\text{O}_6\text{O}'$, for example, will be equivalent to each other as required by $Fd\bar{3}m$.

Despite these constraints, the MEM affords an excellent view of average Bi displacements. No prior description of Bi displacements, or even a knowledge of their existence, is used to produce them in the isosurface neutron density unit cell displayed in Fig. 3(a). Arrows point to the circular Bi density that forms a ring around the $\text{O}'\text{-Bi-O}'$ bond. Two-dimensional slices of the cell viewed along and normal to the $\text{O}'\text{-Bi-O}'$ bond in Figs. 3(b) and 3(c), respectively, show additional detail of the Bi nuclear density. The Bi ring appears hexagonal in Fig. 3(b), which is the required symmetry of the position in $Fd\bar{3}m$. The strongest intensity of Bi points toward the in-plane Ti in Fig. 3(b). This corresponds to a $96h$ site for Bi, not

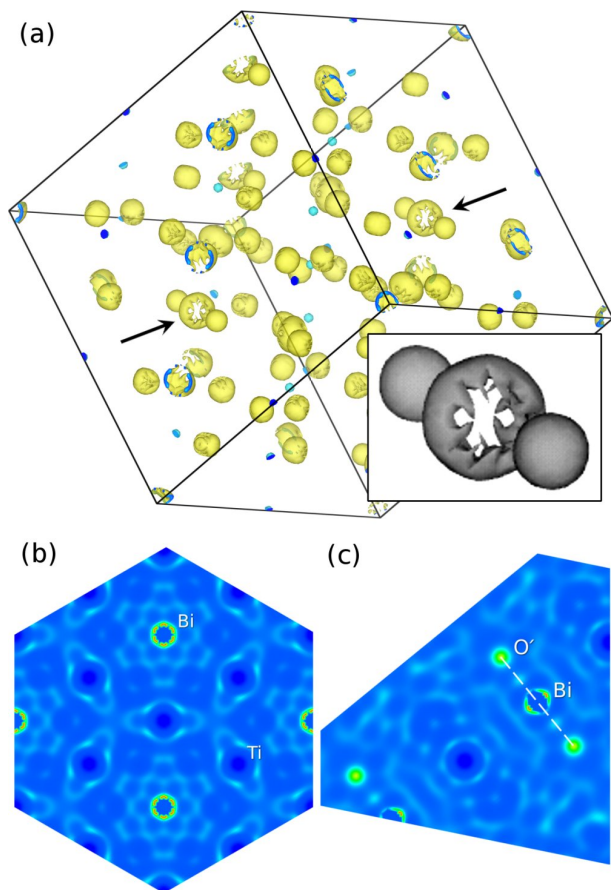


FIG. 3: (Color online) The MEM nuclear density map of the $\text{Bi}_2\text{Ti}_2\text{O}_6\text{O}'$ unit cell at 14 K is plotted in (a). Arrows point to Bi positions where the rings are rotated with the $\text{O}'\text{-Bi-O}'$ direction almost parallel to the viewing direction. The circular Bi isosurface is magnified in the inset. The 2-D density slice in (b) is the $(11\bar{1})$ plane, normal to $\text{O}'\text{-Bi-O}'$ bonds, and (c) is the $(12\bar{1})$ plane with the $\text{O}'\text{-Bi-O}'$ bond dashed. The imposed sixfold symmetry of the Bi ring is evident in the $(11\bar{1})$ slice.

$96g$.⁵⁴ While the Bi shapes found by MEM agree with those from Rietveld refinements, there is no evidence of a tetrapod-shaped spread in the O' density in MEM. This shape would be allowed by symmetry.

C. Least-squares PDF refinement

When displacements of atomic positions and their correlations have been proposed in the pyrochlore structure, it has been compared to the SiO_4 tetrahedral network of β -cristobalite, which is isostructural to the $\text{O}'\text{Bi}_4$ sublattice.^{14,55,56} This configuration would have long-range zig-zag ordering of Bi displacements shown in Fig. 5. These distortions may be ordered along any of the three Bi-Bi directions in the lattice, and the distortions in one direction need not be correlated with those in another.^{23,57} We use least-squares PDF refinement (a

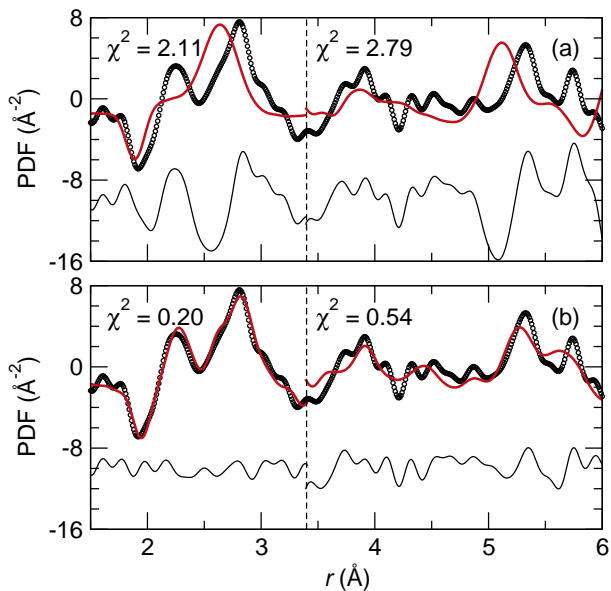


FIG. 4: (Color online) Least-squares refinements of the $\text{Bi}_2\text{Ti}_2\text{O}_6\text{O}'$ PDF at 14 K. Panel (a) shows the fit to an ideal average structure (Bi centered on 16c sites with disc-shaped thermal parameters) as shown in Fig. 1(a). Panel (b) is the Cm structure from first-principles. The χ^2 is shown for two fits per model: a fit up to 3.4 \AA and a fit from 3.4 \AA to 6 \AA . Difference curves are shown below.

small-box technique) to compare the observed local structure to two models: the $Fd\bar{3}m$ Rietveld-derived average model with large ADPs, and the Cm ordered structure from first-principles calculations.

The average model fit to the experimental PDF is shown in Fig. 4(a). The large, disc-shaped ADPs on the Bi positions cause the peak at 2.2 \AA to flatten and disappear, and the fit does not significantly improve as r increases. The short-range fit up to $r = 3.4$ \AA and the medium-range fit from $3.4 \leq r \leq 6$ \AA both give high χ^2 values. The polar, ordered model fit in Fig. 4(b) describes the low- r region very well. Here, a single Bi–O' distance is well-defined, so the peak at 2.2 \AA appears. The medium-range fit is poorer than the short-range fit, but still much better than the average model. From the Rietveld, MEM, and least-squares PDF analyses we know that the structure of $\text{Bi}_2\text{Ti}_2\text{O}_6\text{O}'$ shares some attributes of the average structure (lattice parameters, averaged positions) and the local Cm model (bond distances and angles at low r). Analysis by least-squares refinement of the PDF is limited because we must construct a model that resembles both $Fd\bar{3}m$ and Cm . Due to the complex disorder present in $\text{Bi}_2\text{Ti}_2\text{O}_6\text{O}'$, we conduct reverse Monte Carlo simulations, where large-box models are generated by fits to the data (starting from the ideal structure), and extract statistical measures of these models.

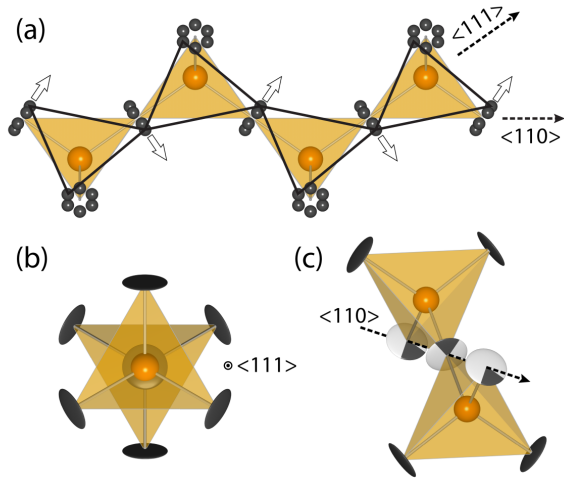


FIG. 5: (Color online) In (a), the ideal $\text{O}'\text{Bi}_4$ sublattice (orange tetrahedra) with split-atom Bi positions (black) can cooperatively order in a zig-zag (arrowed), β -cristobalite-like pattern ordering seen as solid black lines. We use a double-tetrahedral model viewed along the $\text{O}'\text{--O}'$ direction in (b) to investigate local correlations. This shape is viewed in (c) near the Bi–Bi direction with the most probable wedges of the circular Bi ADPs shown schematically for zig-zag ordering.

D. Reverse Monte Carlo simulations

RMC simulations utilize large-box modeling with periodic boundary conditions and are not constrained by symmetry.^{21,42,58} This provides two principal advantages when simulating crystalline materials: the ability to model nuclear positions with arbitrary shapes, and the ability to investigate correlations between atoms on the \AA length-scale. We profit from both when modeling $\text{Bi}_2\text{Ti}_2\text{O}_6\text{O}'$. First, the true shapes of Bi and O' displacements must be elucidated. Second, Bi–Bi nearest-neighbor correlations may lead to cooperative distortions of the $\text{O}'\text{Bi}_4$ sublattice. This type of short-range order would be a signature of local regions where the lone-pair-active Bi displacements effect polar domains.

1. Average atomic displacements

The real-space local structure (coordination environments, short-range correlations, *etc.*) of the RMC supercell are driven by the fit to the PDF, while the Bragg fit constrains the long-range periodicity of the structure (or lack thereof) and ensures reliable displacement parameters. In the case of $\text{Bi}_2\text{Ti}_2\text{O}_6\text{O}'$, we monitor the agreement of Rietveld and RMC ADPs (calculated as the mean-square displacement from ideal positions). RMC simulations were started with the ideal pyrochlore lattice with all Bi atoms on 16c positions. As the simulation progresses, Bi atoms are always observed to move off the central position to form a ring that resembles the Ri-

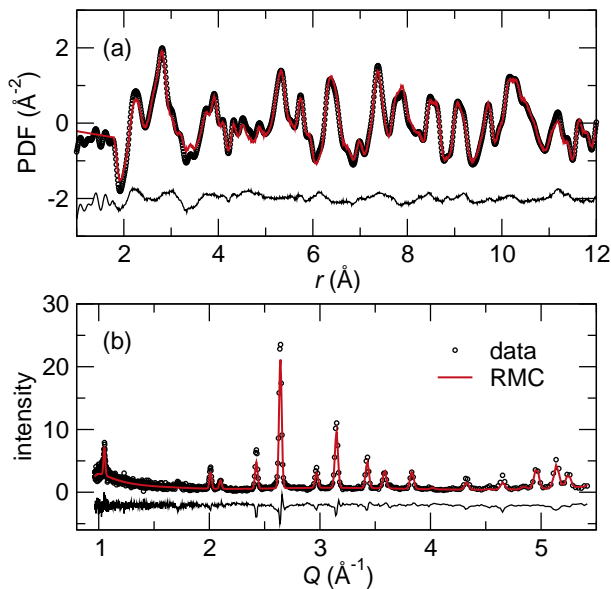


FIG. 6: (Color online) RMC fits to 14 K $\text{Bi}_2\text{Ti}_2\text{O}_6\text{O}'$ experimental data shown for (a) the PDF $G(r)$ and (b) the Bragg profile. The RMC simulations employ supercells ($5 \times 5 \times 5$, $\approx 52 \text{ \AA}$ per side) that fit both data sets simultaneously.

etveld split-atom model. The fits to the 14 K PDF and Bragg profile are shown in Fig. 6(a,b).

A comparison of the ideal unit cell with a folded RMC supercell is shown in Fig. 7. In Fig. 7(b) we fold the 125 unit cells of a supercell into a single unit cell. The result is a cell with “point clouds” on each atomic position that represent a map of the nuclear scattering density on each site in $\text{Bi}_2\text{Ti}_2\text{O}_6\text{O}'$. Of particular note is the large spread of Bi and O' point clouds in Fig. 7(b) in comparison to those of Ti and O. These distributions agree quantitatively with the ADPs from Rietveld refinement.

The $\text{O}'\text{Bi}_4$ sublattice from a 14 K RMC simulation is shown in Fig. 7(c), viewed close to the $\langle 110 \rangle$ direction. From this viewpoint, Bi rings are evident. These rings open normal to the $\text{O}'\text{-Bi-O}'$ bonds, as expected from Rietveld ADPs and MEM. The average shape of a Bi ring is seen in Fig. 8(a). Viewed along the $\text{O}'\text{-Bi-O}'$ direction, it appears circular with a radius of about 0.4 \AA . A histogram of Bi distances from the ideal $16c$ site is given in Fig. 8(c), with a clear maximum at the ring radius. The same procedure applied to O' yields a tetrapodal object. Seen in Fig. 8(b), the arms of this tetrapod point away from the four neighboring Bi atoms. One arm of the tetrapod is in the center of the plot, pointing normal to the page. A key distinction between O' and Bi is that the dense cluster of O' positions is still centered on the ideal $8a$ position, seen as a bright cluster in the center of Fig. 8(b). In contrast, Bi intensity is low at the center and most intensity lies on the ring perimeter. The displacement histograms in Figs. 8(c,d) reveal similar shapes in RMC simulations of 14 K and 300 K data, with a slight broadening at high temperature. This supports the idea

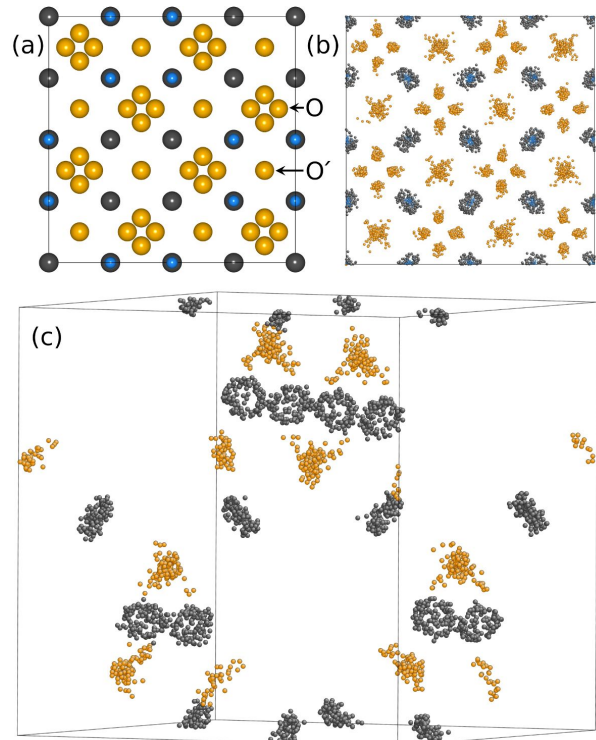


FIG. 7: (Color online) The ideal, isotropic $\text{Bi}_2\text{Ti}_2\text{O}_6\text{O}'$ unit cell is plotted in (a) along the a direction, with Bi atoms in black, Ti blue, and O orange. This unit cell can be visually compared with the folded 14 K RMC supercell in (b). Positional disorder is much greater in Bi and O' (which appear X-shaped in this projection) than in Ti and O (appear as clusters of four O). In (c), the $\text{O}'\text{Bi}_4$ sublattice is plotted near $\langle 110 \rangle$ to show the Bi rings.

that these displacements are frozen at high temperatures and do not fundamentally change with cooling.

The RMC model corroborates with Rietveld and MEM while providing further evidence for a tendency toward a sixfold Bi ring. In Fig. 9(a), a histogram of the rotation angle θ of Bi around the $\langle 111 \rangle$ axis is fit to a sixfold cosine curve. This curve, with a minimum at $\theta = 0^\circ$, corresponds to the $96g$ sites and does not fit the data. Instead, Fig. 9(b) shows excellent agreement between the RMC result and the $96h$ six-fold curve, which is shifted by 30° from $96g$. Note however that the intensity at minima in the curves is not zero; there is still some tendency for Bi to lie at any θ . It is not known whether increased preference for the $96h$ site would push the minima to be nearly zero. It is therefore possible that stronger ordering exists, but is obscured by the resolution of the data.

2. Correlated distortions: double-tetrahedral model

Cooperative β -cristobalite correlations can be visualized in the polyhedral configuration given in Fig. 5. The motif of two corner-linked $\text{O}'\text{Bi}_4$ tetrahedra is the basis

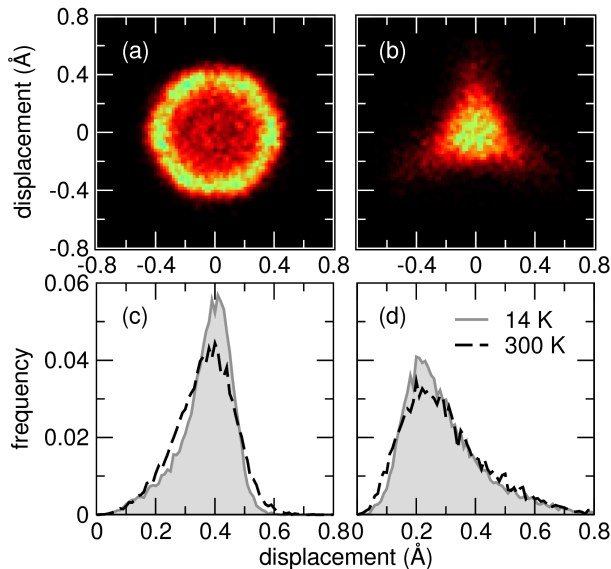


FIG. 8: (Color online) Atomic positions for (a) Bi and (b) O' at 14 K from 14 independent RMC simulations are plotted in the $\{111\}$ plane normal to the $O'-Bi-O'$ bond. Histograms of displacement distances are plotted for 14 K and 300 K simulations in (c) and (d), with the 14 K histograms shaded for clarity. The Bi median displacement of 0.4 Å agrees with the Bi Rietveld ADP.

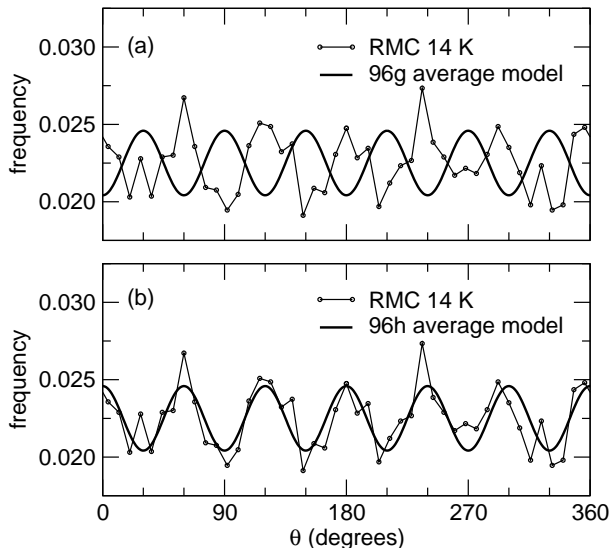


FIG. 9: Histogram of the average Bi displacement angle θ around the $O'-Bi-O'$ bond at 14 K. Solid lines show the expected six-fold cosine curves that indicate preference for (a) 96g or (b) 96h hexagonal ring symmetry.

of our analysis. The zig-zag pattern is comprised of Bi that are all in the same plane (denoted with arrows). This plane is defined by the displacement of any Bi atom in the chain, so the central Bi atom can only participate in zig-zag ordering in one direction at a time. The two inline nearest neighbors of the central atom should have a tendency to displace opposite from the central

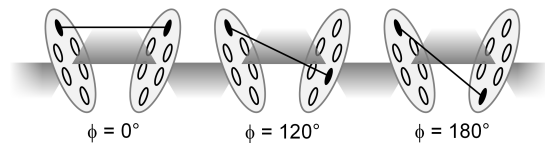


FIG. 10: Schematic of possible values of ϕ , probing nearest-neighbor correlations of Bi displacements (not to scale).

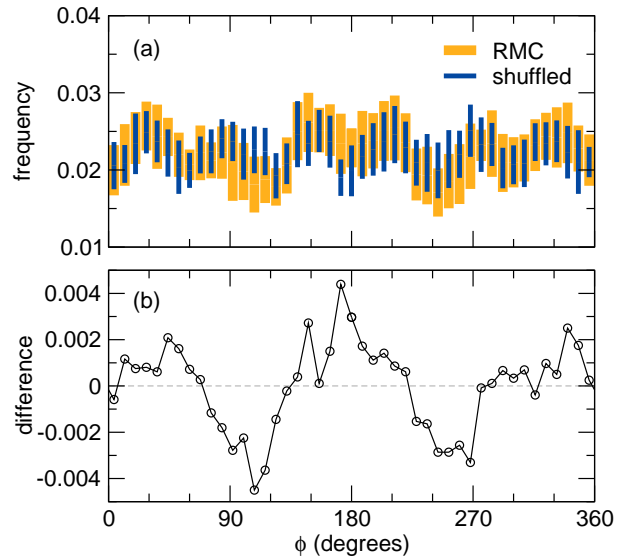


FIG. 11: (Color online) Histograms (a) of the Bi-Bi angle ϕ for neighboring displacements, with error bars of $\pm\sigma$. The difference between the RMC result and the same configurations with randomly shuffled Bi displacements is shown in (b). The difference curve peaks at $\phi = 180^\circ$, indicating some zig-zag-like correlation. Angles around $\phi = 120^\circ$ seem unfavorable.

Bi displacement vector. We can therefore quantify the correlation by examining the angle ϕ between the displacement vector of the central Bi versus the displacement vectors of the two relevant nearest neighbors. Each double-tetrahedral shape in the supercell is examined in this manner. A schematic showing selected orientations of neighboring Bi displacements and their corresponding values of ϕ is given in Fig. 10.

In Fig. 11(a), the relative angle ϕ histogram is plotted for the RMC simulations. It does not have the same six-fold modulation as the averaged Bi angles θ in Fig. 9(b) because ϕ is defined relative to its *neighbors*, while θ is defined relative to the *crystal axes*. We investigate the tendency for ordering by shuffling Bi displacements: the set of all individual Bi displacements from their ideal sites is preserved, but redistributed randomly among the Bi atoms. As a result, their orientations with respect to each other are disrupted. Note that, as a result of the removal of this local correlation, the shuffled ϕ curve is simply a six-fold cosine curve with modulation analogous to θ in Fig. 9(b). The difference between the RMC and shuffled ϕ , plotted in Fig. 11(b), shows a peak at $\phi = 180^\circ$, indicating a preference for zig-zag ordering.

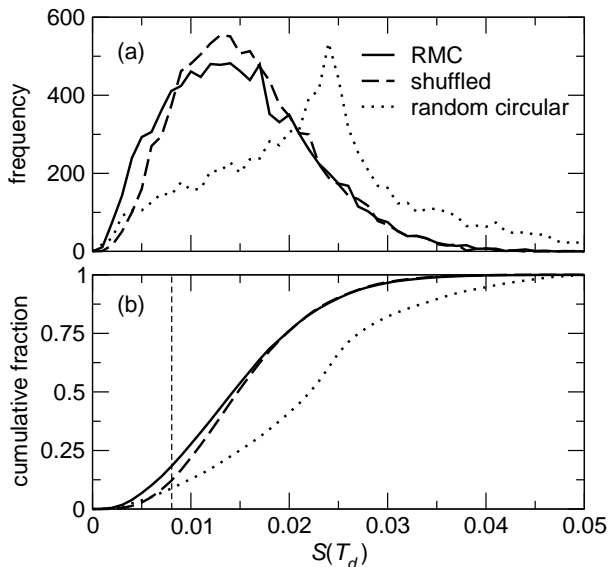


FIG. 12: Histogram (a) of the CSM tetrahedrality $S(T_d)$ for three supercells: the RMC supercell, the same RMC supercell with Bi displacements randomly swapped, and a model with random circular Bi rings of equal radius. The peak at higher $S(T_d)$ in the circular model indicates more deviation from ideality than in the RMC supercells. These histograms are plotted as cumulative probability functions in (b), where the agreement between the RMC and swapped supercells suggest little evidence for cooperative short-range Bi ordering within tetrahedra. A fully-ordered model is denoted by a vertical line at $S(T_d) = 0.008$.

Correlations where $60^\circ < \phi < 120^\circ$ are not preferred. While these results point to anti-alignment of Bi displacements, $\text{Bi}_2\text{Ti}_2\text{O}_6\text{O}'$ should not be considered to follow the β -cristobalite model strictly, since Bi would need to prefer the $96g$ site rather than $96h$.

3. Correlated distortions: continuous symmetry measures

The CSM provides a quantitative measure of a polyhedron’s distortion, in the form of a “distance” from ideality.^{26–28} In our case, a perfect tetrahedron would have tetrahedrality $S(T_d) = 0$, while distortions from ideality increase this value toward 1. As a point of reference, the Jahn-Teller distorted CuO_4 tetrahedron in CuMn_2O_4 ²⁵ has $S(T_d) = 0.0235$ while a square plane has $S(T_d) = \frac{1}{3}$.

Application of CSM to the $\text{O}'\text{Bi}_4$ sublattice is useful because $S(T_d)$ describes the correlations between four neighboring Bi atoms. Comparison between models and RMC simulations are shown in Fig. 12. For a model with ordered β -cristobalite-type ordering with a similar displacement magnitude, $S(T_d) = 0.008$. This is plotted as a vertical line in Fig. 12(b). In contrast, uncorrelated and evenly circular (with radius 0.4 \AA) Bi displacements produce a wide distribution of $S(T_d)$, shown as a dotted

line in Fig. 12(a), and again as a cumulative fraction in Fig. 12(b).

In a case where zig-zag (or otherwise correlated) distortions are present on most $\text{O}'\text{Bi}_4$ tetrahedra in the supercell, we expect Bi displacements to be correlated with their nearest neighbors, and a polyhedral rigidity reminiscent of SiO_4 tetrahedra might exist. If these displacements from ideal positions were randomly swapped among Bi atoms, the ordering would be destroyed and $S(T_d)$ would increase toward the random circular model. In a case where there is no short-range Bi–Bi ordering, randomly swapping the displacements should have no effect on the $S(T_d)$ distribution.

In Fig. 12 we compare the $S(T_d)$ distributions for the RMC supercell and the same supercell with Bi displacements randomly swapped. The distributions are shown as histograms of $S(T_d)$ in (a) and cumulative fractions in (b). The random swapping slightly increases $S(T_d)$ for the RMC supercell, seen as a shift to the right in Fig. 12(b). This curve is still quite separated from the random circular model.

Two aspects of the Bi distribution can be gleaned from this comparison. First, the Bi displacements of the RMC supercell are more strongly tetrahedral than the random circular model. This could be due to rigidity of the $\text{O}'\text{Bi}_4$ tetrahedra, or the fact that the RMC has a distribution of Bi displacements [Fig. 8(c)] whereas the circular model has strictly $r = 0.4 \text{ \AA}$. The separation between RMC and shuffled CSM points to rigidity that may be explained by correlated Bi displacements. Just as shuffling Bi displacements disrupts the ordering between *pairs* of Bi as viewed by ϕ in Fig. 11(b), it also disrupts ordering between sets of *four* Bi displacements as viewed by CSM in Fig. 12(b).

IV. CONCLUSIONS

We have shown that a structural investigation of the strongly disordered pyrochlore $\text{Bi}_2\text{Ti}_2\text{O}_6\text{O}'$ benefits from modeling real- and reciprocal space structure simultaneously. The combination of Rietveld refinement, MEM, least-squares PDF refinement, and RMC simulations provide a description of the structure over many length scales. Of particular interest is the behavior of the displaced lone-pair active Bi^{3+} cation. Average structure models indicate a preference for static displacements. MEM and RMC show that Bi prefers the $96h$ (pointing between nearby O from the TiO_6 sublattice) rather than $96g$ sites (pointing toward neighboring O). Statistical measures of these displacements are extracted from RMC supercells.

RMC simulations show that Bi displacements lie at all angles θ in a ring normal to the $\text{O}'\text{–Bi–O}'$ bond with radius $r \sim 0.4 \text{ \AA}$, but there is a preference for θ corresponding to $96h$ positions. O' atoms are centered on the ideal site, but in a tetrapodal shape with arms pointing away from neighboring Bi. Comparing the RMC result with an identical supercell with shuffled Bi displacements reveals

that neighboring Bi displacements show some correlation with each other, with a preference for $\phi = 180^\circ$ alignment. This corresponds to a zig-zag type ordering that merits further investigation. Measures of the tetrahedrality $S(T_d)$ of the O/Bi_4 sublattice indicate that neighboring displacements are weakly correlated, thus the sublattice may exhibit some rigidity.

V. ACKNOWLEDGMENTS

We thank M. Pinsky and D. Avnir for providing the CSM script, and we thank K. L. Page, R. L. Withers,

M. G. Tucker, and A. L. Goodwin for helpful discussions. This work was supported by the Institute for Multiscale Materials Studies and the National Science Foundation through a Career Award (DMR 0449354) to RS and MRSEC facilities (DMR 0520415). Neutron scattering was performed on NPDF at the Lujan Center at the Los Alamos Neutron Science Center, funded by the DOE Office of Basic Energy Sciences. Los Alamos National Laboratory is operated by Los Alamos National Security, LLC under DOE Contract DE-AC52-06NA25396.

-
- * Electronic address: dshoe@mrl.ucsb.edu
- ¹ A. P. Ramirez, *Ann. Rev. Mater. Sci.* **24**, 453 (1994).
 - ² A. P. Ramirez, A. Hayashi, R. J. Cava, R. Siddharthan, and B. S. Shastry, *Nature* **399**, 333 (1999).
 - ³ D. J. P. Morris, D. A. Tennant, S. A. Grigera, B. Klemke, C. Castelnovo, R. Moessner, C. Czternasty, M. Meissner, K. C. Rule, J. Hoffmann, et al., *Science* **326**, 411 (2009).
 - ⁴ H. Kadowaki, N. Doi, Y. Aoki, Y. Tabata, T. J. Sato, J. W. Lynn, K. Matsuhira, and Z. Hiroi, *J. Phys. Soc. Japan* **78**, 103706 (2009).
 - ⁵ S. Yonezawa, Y. Muraoka, and Z. Hiroi, *J. Phys. Soc. Japan* **73**, 1655 (2004).
 - ⁶ C. A. Kendziora, I. A. Sergienko, R. Jin, J. He, V. Koppens, B. C. Sales, and D. Mandrus, *Phys. Rev. Lett.* **95**, 125503 (2005).
 - ⁷ S. Onoda and N. Nagaosa, *Phys. Rev. Lett.* **90**, 196602 (2003).
 - ⁸ R. Seshadri, *Solid State Sci.* **8**, 259 (2006).
 - ⁹ A. L. Hector and S. B. Wiggins, *J. Solid State Chem.* **177**, 139 (2004), ISSN 0022-4596.
 - ¹⁰ N. A. Hill, *Ann. Rev. Mater. Res.* **32**, 1 (2002).
 - ¹¹ B. C. Melot, R. Tackett, J. O'Brien, A. L. Hector, G. Lawes, R. Seshadri, and A. P. Ramirez, *Phys. Rev. B* **79**, 224111 (2009).
 - ¹² C. J. Fennie, R. Seshadri, and K. M. Rabe, 0712.1846 (2007), URL <http://arxiv.org/abs/0712.1846>.
 - ¹³ R. L. Withers, T. R. Welberry, A. K. Larsson, Y. Liu, L. Norn, H. Rundlf, and F. J. Brink, *J. Solid State Chem.* **177**, 231 (2004), ISSN 0022-4596.
 - ¹⁴ A. L. Goodwin, R. L. Withers, and H. Nguyen, *J. Phys. Cond. Mat.* **19**, 335216 (2007).
 - ¹⁵ Y. Liu, R. L. Withers, H. B. Nguyen, K. Elliott, Q. Ren, and Z. Chen, *J. Solid State Chem.* **182**, 2748 (2009).
 - ¹⁶ Y. Tabira, R. L. Withers, T. Yamada, and N. Ishizawa, *Z. Kristallogr.* **216**, 92 (2001).
 - ¹⁷ T. Egami and S. J. L. Billinge, *Underneath the Bragg Peaks, Volume 7: Structural Analysis of Complex Materials* (Pergamon, 2003), ISBN 0080426980.
 - ¹⁸ T. Proffen, cond-mat/0002388 (2000), URL <http://arxiv.org/abs/cond-mat/0002388>.
 - ¹⁹ R. L. McGreevy and L. Pusztai, *Mol. Simulat.* **1**, 359 (1988).
 - ²⁰ R. L. McGreevy, *J. Phys. Cond. Mat.* **13**, R877 (2001).
 - ²¹ M. G. Tucker, M. T. Dove, and D. A. Keen, *J. Appl. Cryst.* **34**, 630 (2001).
 - ²² A. Sartbaeva, S. A. Wells, M. F. Thorpe, E. S. Bozin, and S. J. L. Billinge, *Phys. Rev. Lett.* **99**, 155503 (2007).
 - ²³ M. G. Tucker, M. P. Squires, M. T. Dove, and D. A. Keen, *J. Phys. Cond. Mat.* **13**, 403 (2001).
 - ²⁴ S. Adams and J. Swenson, *J. Phys. Cond. Mat.* **17**, S87 (2005).
 - ²⁵ D. P. Shoemaker, J. Li, and R. Seshadri, *J. Am. Chem. Soc.* **131**, 11450 (2009).
 - ²⁶ H. Zabrodsky, S. Peleg, and D. Avnir, *J. Am. Chem. Soc.* **114**, 7843 (1992).
 - ²⁷ M. Pinsky and D. Avnir, *Inorg. Chem.* **37**, 5575 (1998).
 - ²⁸ S. Keinan and D. Avnir, *J. Chem. Soc., Dalton Trans.* pp. 941-947 (2001).
 - ²⁹ D. Yogeve-Einot and D. Avnir, *Acta Cryst. B* **60**, 163 (2004), ISSN 0108-7681.
 - ³⁰ K. M. Ok, P. S. Halasyamani, D. Casanova, M. Llunell, P. Alemany, and S. Alvarez, *Chem. Mater.* **18**, 3176 (2006).
 - ³¹ J. D. Bernal and R. H. Fowler, *J. Chem. Phys.* **1**, 515 (1933).
 - ³² A. Larson and R. Von Dreele, Los Alamos National Laboratory Report LAUR **86**, 748 (2000).
 - ³³ P. F. Peterson, M. Gutmann, T. Proffen, and S. J. L. Billinge, *J. Appl. Cryst.* **33**, 1192 (2000).
 - ³⁴ C. L. Farrow, P. Juhas, J. W. Liu, D. Bryndin, E. S. Bozin, J. Bloch, T. Proffen, and S. J. L. Billinge, *J. Phys. Cond. Mat.* **19**, 335219 (2007).
 - ³⁵ G. Kresse and J. Hafner, *Phys. Rev. B* **47**, 558 (1993).
 - ³⁶ G. Kresse and J. Furthmüller, *Phys. Rev. B* **54**, 11169 (1996).
 - ³⁷ P. Blöchl, *Phys. Rev. B* **50**, 17953 (1994).
 - ³⁸ G. Kresse and D. Joubert, *Phys. Rev. B* **59**, 1758 (1999).
 - ³⁹ *Bilbao crystallographic server*, <http://www.cryst.ehu.es>.
 - ⁴⁰ D. M. H. H. T. Stokes and B. J. Campbell, *Isotropy* (2007), <http://stokes.byu.edu/isotropy.html>.
 - ⁴¹ F. Izumi and A. Dilanian, *Recent Research Developments in Physics*, vol. 3 (Transworld Research Network, Trivandrum, India, 2002), ISBN 81-7895-046-4.
 - ⁴² M. G. Tucker, D. A. Keen, M. T. Dove, A. L. Goodwin, and Q. Hui, *J. Phys. Cond. Mat.* **19**, 335218 (2007).
 - ⁴³ D. A. Keen, *J. Appl. Cryst.* **34**, 172 (2001).
 - ⁴⁴ K. Momma and F. Izumi, *J. Appl. Cryst.* **41**, 653 (2008).
 - ⁴⁵ J. Li, *Modelling and Simul. Mater. Sci. Eng.* **11**, 173 (2003).
 - ⁴⁶ I. Radosavljevic, J. S. O. Evans, and A. W. Sleight, *J. Solid State Chem.* **136**, 63 (1998).

- ⁴⁷ I. R. Evans, J. A. K. Howard, and J. S. O. Evans, *J. Mater. Chem.* **13**, 2098 (2003).
- ⁴⁸ J. Cagnon, D. S. Boesch, N. H. Finstrom, S. Z. Nergiz, S. P. Keane, and S. Stemmer, *J. Appl. Phys.* **102**, 044102 (2007).
- ⁴⁹ E. T. Jaynes, *Phys. Rev.* **106**, 620 (1957).
- ⁵⁰ E. T. Jaynes, *Phys. Rev.* **108**, 171 (1957).
- ⁵¹ M. Sakata and M. Sato, *Acta Cryst. A* **46**, 263 (1990).
- ⁵² M. Sakata, R. Mori, S. Kumazawa, M. Takata, and H. Toraya, *J. Appl. Cryst.* **23**, 526 (1990).
- ⁵³ S. Kumazawa, Y. Kubota, M. Takata, M. Sakata, and Y. Ishibashi, *J. Appl. Cryst.* **26**, 453 (1993).
- ⁵⁴ M. Avdeev, M. K. Haas, J. D. Jorgensen, and R. J. Cava, *J. Solid State Chem.* **169**, 24 (2002).
- ⁵⁵ Y. Tabira, R. Withers, J. Thompson, and S. Schmid, *J. Solid State Chem.* **142**, 393 (1999).
- ⁵⁶ B. Nguyen, Y. Liu, and R. L. Withers, *J. Solid State Chem.* **180**, 549 (2007).
- ⁵⁷ R. Withers, J. Thompson, and T. Welberry, *Phys. Chem. Miner.* **16**, 517 (1989).
- ⁵⁸ T. Proffen and T. R. Welberry, *Acta Cryst. A* **53**, 202 (1997).